Dynamic Fragmentation of Brittle Materials: Analytical Mechanics-Based Models

W.J. Drugan

January 2001

UWFDM-1149

Accepted for publication in the *Journal of the Mechanics and Physics of Solids.*

FUSION TECHNOLOGY INSTITUTE

UNIVERSITY OF WISCONSIN

MADISON WISCONSIN

Dynamic Fragmentation of Brittle Materials: Analytical Mechanics-Based Models

W.J. Drugan

Fusion Technology Institute
Department of Engineering Physics
University of Wisconsin-Madison
1500 Engineering Drive
Madison, WI 53706

drugan@engr.wisc.edu

January 2001

UWFDM-1149

Accepted for publication in the *Journal of the Mechanics and Physics of Solids*.

ABSTRACT

Two analytical mechanics-based models of dynamic fragmentation in brittle materials are proposed and solved to predict fragment size and time to fragmentation onset in terms of fundamental material properties and the applied strain rate. Previous widely-adopted analytical models of dynamic fragmentation are based on relatively simple energy balance arguments, and assume that the fragmentation event occurs instantaneously. The present models account for the actual time-varying dynamic deformation that occurs prior to fragmentation onset. One of the models treats the fragmenting material as initially flaw-free, and determines the minimum fragment size predicted by a dynamic instability analysis. The second model accounts for initial flaw spacing (which may correlate physically with, for example, grain size), and a dynamic instability analysis is employed to determine which flaws become critical. The fragment size predictions of the present models and two previous energy-based models are found to agree at extremely high strain rates ($\approx 5 \times 10^7$ s^{-1} for dense alumina), but the present, more realistic analysis indicates that the regime of validity of the energy-based models is rather restricted. The predictions of the present models are also shown to agree with those of a recent numerical finite element simulation of dynamic fragmentation which applies to a lower strain rate regime. Comparisons of the two new models show that if a material contains initial flaws whose spacing is smaller than the predicted fragment size of an equivalent "unflawed" material, the fragment size of the preflawed material will be smaller in general, but usually not as small as the initial flaw spacing. The analysis also permits determination of the evolution of the strain rate distribution in a prospective fragment before and after fragmentation initiation; results are presented for some example cases. Finally, closed-form analytical results are derived for minimum fragment size and time to fragmentation for strain rates in the quasi-static regime; these show the fragment size to be independent of strain rate in this regime, and the time to fragmentation initiation to be inversely proportional to the strain rate.

1. INTRODUCTION

Many brittle materials (and several nominally ductile ones) fail by fragmentation into numerous pieces when subjected to rapid energy input. Such rapid energy input may be due to impact with or by another body, high-energy radiation provided e.g. by lasers or x-rays, rapid temperature change, impingement of a shock wave, etc. Usually one wishes to prevent fragmentation or, if it is unavoidable, to control it for safety reasons; however, there are also applications, such as mining, in which one desires to cause fragmentation in the most efficient and controlled manner possible. These examples and others motivate study and modeling of dynamic fragmentation, the fundamental mechanics of which has received relatively scant treatment.

The dynamic fragmentation of brittle materials is an extremely complex process involving the nucleation and propagation of myriad microcracks that finally coalesce, breaking the solid into fragments. To date, the most widely applied theoretical models of the process, e.g. those based on the pioneering studies of Grady (1982) and Glenn and Chudnovsky (1986), involve some type of relatively simple global energy balance argument to predict fragment sizes and velocities. These models essentially assume that the energy available to form new fracture surfaces causes these to form instantaneously; thus, these models are expected to be accurate at extremely high strain rates, when the time to fragmentation is extremely short. However, the models themselves are not able to estimate their regimes of validity.

Very recently, computational modeling of dynamic fragmentation has been carried out by large numerical finite element simulations, in an attempt to analyze the dynamic deformations that occur before and during fragmentation. These computations are based on the incorporation of cohesive surfaces between standard elastic elements, to serve as prospective fracture paths in a dynamic simulation. Examples of such work include that of Camancho and Ortiz (1996), Espinosa et al. (1998) and Miller et al. (1999).

The purpose of the present study is to introduce and analyze two simple analytical mechanics-based models of the dynamic fragmentation process which, rather than employing a global energy balance, model the actual ongoing dynamic

deformation and the development of fracture surfaces. At the same time, we attempt to obtain analytical results to the fullest possible extent, and beyond this perform a minimum amount of numerical analysis. The key feature of the approach is to analyze the time-varying dynamic deformation of a prospective brittle fragment that is joined by nonlinear cohesive zones to the rest of the body; the cohesive zones model, in a manner determined by previous *ab initi*o atomistic simulations, the separation of atomic planes. This leads to predictions of time to initiate fragmentation and the minimum fragment size, as a function of material properties and the applied strain rate. In one model, the brittle solid is idealized as being initially flaw-free, but flaws are assumed to nucleate at the times and locations predicted by a dynamic instability analysis. The second model treats situations in which a body contains pre-existing flaws, and dynamic instability analysis is applied to determine which of these become critical and when.

These models provide results over a large range of applied strain rates, and hence are capable of delineating quantitatively the range of validity of the widely-adopted energy-based models of Grady (1982) and Glenn and Chudnovsky (1986). The conclusion is that the energy-based models appear to have a rather small regime of validity that is restricted to extremely high applied strain rates. The results of the new models are also compared, and shown to agree, with the recent numerical finite element simulations of Miller et al. (1999), which treated applied strain rates that are orders of magnitude lower than the very high strain rate regime of applicability of the energy-based models.

We also provide a separate analysis of the quasi-static regime, in which applied strain rates are sufficiently low that material inertia effects are negligible. Closed-form analytical results are obtained for the minimum fragment size and time to fragmentation initiation; these results show that the minimum fragment size becomes independent of applied strain rate in the quasi-static regime, and the time to fragmentation initiation becomes proportional to the inverse of the applied strain rate.

2. FORMULATION: ONE-DIMENSIONAL MODELS

In order to convey ideas and assumptions clearly, we first formulate and solve one-dimensional versions of our models. Later we show that the results of these one-dimensional models are directly applicable to the three-dimensional case. The models will involve a dynamic analysis of the deformation of a prospective brittle fragment; this section develops the formulation common to both models.

Consider an infinitely long bar of brittle elastic material that is permitted to deform only in the direction of the bar's axis, so that the bar experiences one-dimensional plane strain in the x, y plane; that is, only x-direction displacements are permitted. In this first analysis, we follow Grady (1982) and assume that the bar is in a state of rapid uniform expansion, so that the strain rate is constant throughout the bar. This assumption is appropriate for situations in which a body has experienced a rapid, uniform energy input, such as from x-rays, and represents perhaps the simplest situation for fragmentation analysis. The ensuing analysis will make clear that other loading situations can be treated within the formulation to be presented by applying different boundary and initial conditions.

Alternatively, a bar of finite length that experiences the same conditions as those just described is illustrated in Figure 1. The boundary conditions on this bar are thus that the shear traction is zero on all boundaries, the normal velocity is zero on $y = \pm h/2$, and the normal velocity is constant and uniform on $x = \pm L/2$ and in accord with the constant strain rate; also in accord with this is the initial condition of x-direction velocity that varies linearly with x.

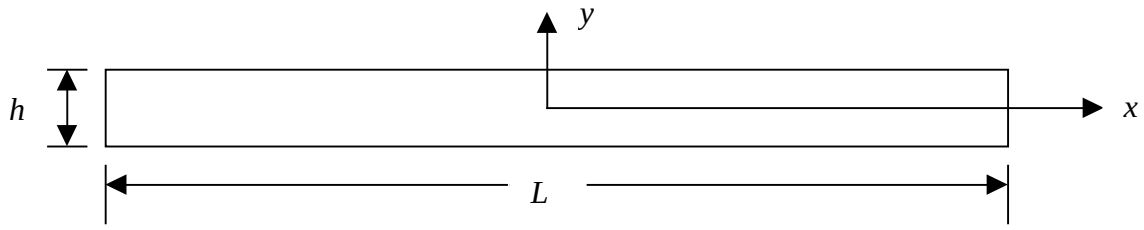

Figure 1. Bar of brittle elastic material experiencing a rapid, uniform x-direction strain rate.

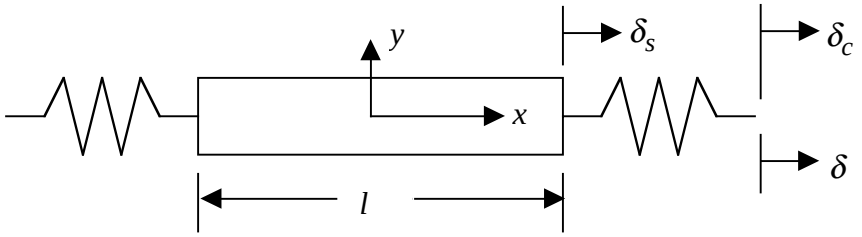

Figure 2. A prospective fragment, consisting of an elastic segment of length l and two half cohesive zones.

Let us focus attention on one prospective fragment inside the bar. We shall now choose the coordinate system to be centered in this fragment, as shown in Figure 2. As illustrated there, the fragment consists of an elastic segment of length l, joined by cohesive surfaces to neighboring fragments; half of each cohesive surface is illustrated. We define δ_s to be the displacement of the elastic segment end relative to its center, δ_c to be the displacement of half the cohesive zone relative to the segment end; the total relative displacement, δ, is thus $\delta = \delta_s + \delta_c$.

We shall solve the elastodynamic governing equations for the fields inside the elastic segment, subject to the appropriate boundary conditions, to be discussed. The displacement and velocity fields in the segment will be understood to be relative to those of the segment center.

The three-dimensional version of Hooke's law for a homogeneous, isotropic linear elastic solid is:

$$\sigma_{ij} = \frac{E}{1+\nu}\left(\varepsilon_{ij} + \frac{\nu}{1-2\nu}\varepsilon_{kk}\delta_{ij}\right), \tag{1}$$

where E is Young's modulus, ν is Poisson's ratio, σ_{ij} and ε_{ij} are components of the stress and infinitesimal strain tensors, respectively, δ_{ij} is the Kronecker delta, and a repeated index implies summation. Since we permit only x-direction deformations, $\varepsilon_{yy} = \varepsilon_{zz} = 0$, so that (1) gives

$$\sigma_{xx} = \frac{E(1-\nu)}{(1+\nu)(1-2\nu)}\varepsilon_{xx} \equiv \hat{E}\varepsilon_{xx}, \tag{2}$$

the last equation in (2) defining the effective one-dimensional tensile modulus $\hat{E}$.

The nontrivial equation of conservation of linear momentum is:

$$\frac{\partial \sigma_{xx}}{\partial x} = \rho \frac{\partial^2 u}{\partial t^2} \tag{3}$$

where ρ is mass density, t is time and u is the x-direction component of displacement (relative to the displacement of the segment center). From (2) and the definition of infinitesimal strain (i.e., compatibility),

$$\sigma_{xx} = \hat{E}\varepsilon_{xx} = \hat{E}\frac{\partial u}{\partial x}, \tag{4}$$

substitution of which into (3) gives

$$c^2 \frac{\partial^2 u}{\partial x^2} = \frac{\partial^2 u}{\partial t^2}, \quad \text{where} \quad c \equiv \sqrt{\frac{\hat{E}}{\rho}}. \tag{5}$$

The general solution to (5) is

$$u(x,t) = f(x - ct) + g(x + ct), \tag{6}$$

where f and g are arbitrary functions, to be determined by the boundary and initial conditions, and c is the elastic wave speed defined in (5).

The initial conditions in accord with the Grady assumption are those of zero displacement and a uniform strain rate, which corresponds to a linear velocity distribution:

$$u(x,0) = 0, \qquad \frac{\partial u}{\partial t}(x,0) = \dot{\varepsilon}_0 \, x, \tag{7}$$

where $\dot{\varepsilon}_0$ is the uniform applied strain rate. Application of (7) to (6) permits determination of f and g, so that (6) is

$$u(x,t) = \frac{\dot{\varepsilon}_0}{4c}\left[(x + ct)^2 - (x - ct)^2\right]. \tag{8}$$

This is valid in the triangular Region A in the x, t plane illustrated in Figure 3.

From (6) and (8), the solution in Region B of Figure 3 is:

$$u(x,t) = -\frac{\dot{\varepsilon}_0}{4c}(x - ct)^2 + G(x + ct), \tag{9}$$

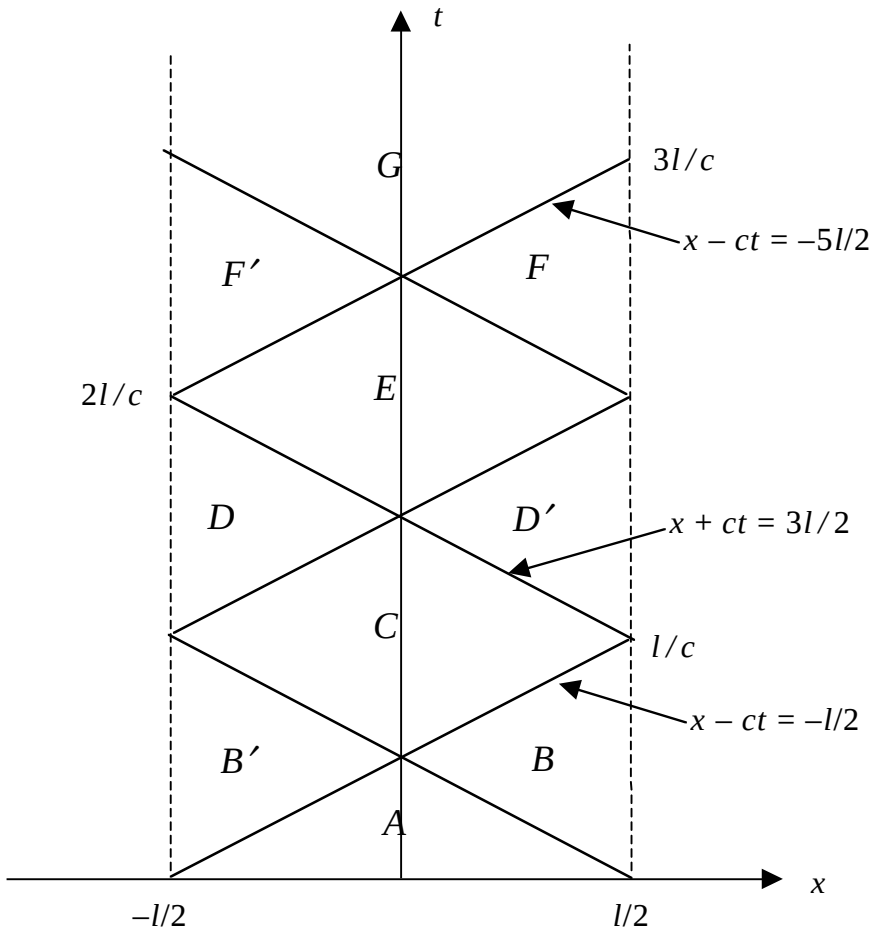

Figure 3. Plot of location x within the elastic segment of Figure 2 versus time. The slanted lines are characteristics of the partial differential equation (5), delineating solution regimes labeled by uppercase letters.

where G is an as-yet undetermined function, which is found by enforcing the appropriate boundary conditions on the $x = l/2$ end of the elastic segment. These conditions are stress continuity and geometrical compatibility (i.e., displacement continuity) with the cohesive surface.

We assume that the bar of brittle material experiences a uniform constant strain rate $\dot{\varepsilon}_{xx} = \dot{\varepsilon}_o$ until fragmentation initiates. [It is not known *a priori* how this strain rate is apportioned between the elastic segment and the cohesive zones of a prospective fragment; the ensuing analysis determines this.] This implies that the time rate of the total relative displacement δ defined in Figure 2 should be

$$\delta'(t) = \dot{\varepsilon}_o \frac{l}{2} \quad \Rightarrow \quad \delta(t) = \dot{\varepsilon}_o \frac{l}{2} t\,, \tag{10}$$

where the second equation is the time-integral of the first, with the integration constant set equal to zero since we require that $\delta(0) = 0$. Now, using (10) and the definition of δ, continuity of displacement between the elastic segment and the cohesive zone requires:

$$u\left(\frac{l}{2}, t\right) = \delta_s(t) = \delta(t) - \delta_c(t) = \dot{\varepsilon}_0 \frac{l}{2} t - \delta_c(t). \tag{11}$$

The cohesive zone is assumed to have a stress-displacement relation of the form (recalling that δ_c is *half* the cohesive zone displacement):

$$\sigma_c = F\left(2\delta_c\right). \tag{12}$$

Thus, employing (4) and (12), normal stress continuity between the elastic segment and the cohesive zone requires

$$\hat{E}\frac{\partial u}{\partial x}\left(\frac{l}{2}, t\right) = F\left(2\delta_c(t)\right). \tag{13}$$

Substitution of the Region B solution form (9) into the boundary conditions (11) and (13) gives two equations for the two unknown functions $G(\xi)$ and $\delta_c(t)$:

$$-\frac{\dot{\varepsilon}_0}{4c}\left(\frac{l}{2} - ct\right)^2 + G\left(\frac{l}{2} + ct\right) = \dot{\varepsilon}_0 \frac{l}{2} t - \delta_c(t) \tag{14a}$$

$$\hat{E}\left[-\frac{\dot{\varepsilon}_0}{2c}\left(\frac{l}{2} - ct\right) + G'\left(\frac{l}{2} + ct\right)\right] = F\left(2\delta_c(t)\right). \tag{14b}$$

By taking the time derivative of (14a) and using the result to eliminate G' in (14b), one obtains a differential equation for $\delta_c(t)$:

$$\delta_c'(t) + \frac{c}{\hat{E}} F\left(2\delta_c(t)\right) = c\,\dot{\varepsilon}_0\, t, \qquad \delta_c(0) = 0. \tag{15}$$

Recall from Figure 3 and Equation (9) that (15) is valid for $0 \le t \le l/c$.

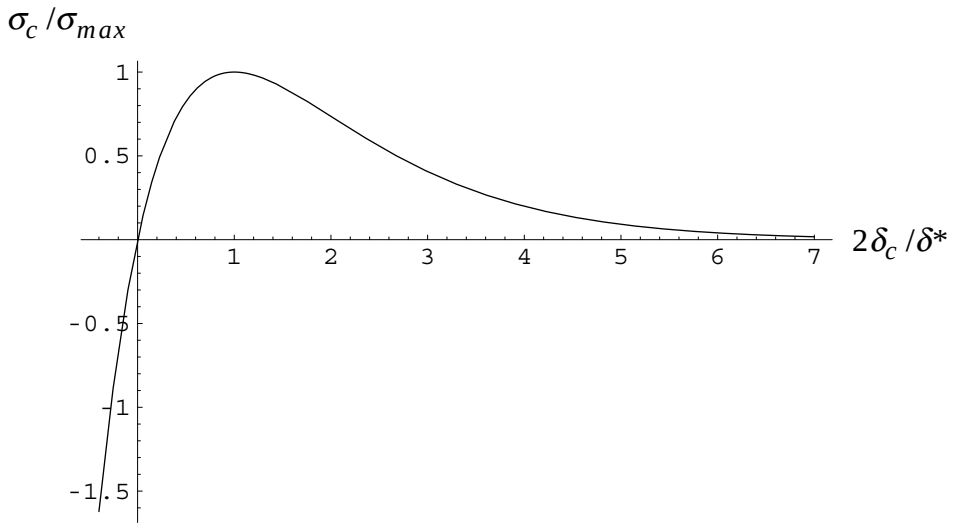

Figure 4. The cohesive zone normal stress–normal separation relation (16).

Rose et al. (1981, 1983) have performed ab initio atomistic calculations that suggest – at least for metals – a universal exponential form for the normal traction versus normal separation relation for atomistically sharp interfaces, which we shall assume here for the anticipated brittle fracturing. Their work implies that the cohesive zone stress-displacement relation (12) has the form:

$$\sigma_c(2\delta_c) = \sigma_{\max} \frac{2\delta_c}{\delta^*} \exp\left(1 - \frac{2\delta_c}{\delta^*}\right). \tag{16}$$

Here, σ_{max} is the strength of the cohesive surface, which is attained when $2\delta_c = \delta^*$. Equation (16) is plotted in Figure 4.

For this cohesive zone model, (15) becomes:

$$\boxed{\delta_c'(t) + \frac{1}{\tau}\delta_c(t)\exp\left[1 - \frac{2}{\delta^*}\delta_c(t)\right] = c\,\dot{\varepsilon}_0\,t, \quad \delta_c(0) = 0, \qquad \text{valid for } \ 0 \le t \le \frac{l}{c}}, \tag{17}$$

where we have defined the following constant having time dimensions

$$\tau \equiv \frac{\delta^* \hat{E}}{2c\sigma_{\max}}. \tag{18}$$

We have emphasized that (17) is valid for $0 \le t \le l/c$. For situations in which fragmentation onset does not occur within this time range, we must derive a differential equation for $\delta_c(t)$ valid for longer times, i.e., for $t > l/c$. Figure 3 shows that for $l/c \le t \le 2l/c$, we will need a representation of the displacement field in Region D. This is obtained by recalling that the solution must have the general form (6), and that the second function in this form in Region D will be identical to the function $G(x + ct)$ of Region B. Function G of Region B is given by (14a), which after some manipulation gives:

$$G(\xi) = \frac{\dot{\varepsilon}_0}{4c}\xi^2 - \delta_c^{(1)}\left(\frac{1}{c}\left(\xi - \frac{l}{2}\right)\right), \tag{19}$$

where $\delta_c^{(1)}(t)$ is the solution to (17). Then, employing (6), the solution in Region D of Figure 3 is:

$$u(x,t) = \frac{\dot{\varepsilon}_0}{4c}(x+ct)^2 - \delta_c^{(1)}\left(\frac{1}{c}\left(x - \frac{l}{2} + ct\right)\right) + H(x-ct), \tag{20}$$

where H is an as-yet undetermined function.

To derive a differential equation for $\delta_c(t)$ valid for $l/c \le t \le 2l/c$, we now employ (20) and enforce stress and displacement continuity with the cohesive zone at $x = -l/2$, in a manner similar to the preceding analysis that lead to (11) and (13). This leads to two equations for the two unknowns $H(\xi)$ and $\delta_c(t)$:

$$-\frac{\dot{\varepsilon}_0}{4c}\left(ct - \frac{l}{2}\right)^2 + \delta_c^{(1)}\left(t - \frac{l}{c}\right) - H\left(-\frac{l}{2} - ct\right) = \dot{\varepsilon}_0 \frac{l}{2} t - \delta_c(t) \tag{21a}$$

$$\frac{\dot{\varepsilon}_0}{2c}\left(ct - \frac{l}{2}\right) - \frac{1}{c}\delta_c^{(1)\prime}\left(t - \frac{l}{c}\right) + H'\left(-\frac{l}{2} - ct\right) = \frac{\sigma_{\max}}{\hat{E}}\frac{2\delta_c}{\delta^*}\exp\left(1 - \frac{2\delta_c}{\delta^*}\right). \tag{21b}$$

By taking the time derivative of (21a) and using the result to eliminate H' in (21b), one obtains the following differential equation for $\delta_c(t)$:

$$\boxed{\delta_c'(t)+\frac{\delta_c(t)}{\tau}\exp\left(1-\frac{2\delta_c(t)}{\delta^*}\right)=c\,\dot{\varepsilon}_0\,t-2\delta_c^{(1)\prime}\left(t-\frac{l}{c}\right),\quad \text{valid for } \frac{l}{c}\le t\le 2\frac{l}{c}} \tag{22a}$$

to be solved with the initial condition:

$$\boxed{\delta_c\left(\frac{l}{c}\right)=\delta_c^{(1)}\left(\frac{l}{c}\right)}. \tag{22b}$$

For fragmentation occurring at times longer than the range given in (22a), one performs an analysis very similar to that above. For example, to derive the differential equation governing $\delta_c(t)$ in the range $2l/c \le t \le 3l/c$, we need the displacement field solution in Region F of Figure 3. This will have the form (6), with the first function being $H(x - ct)$ of Region D, which is solved for from (21a). As above, one then enforces stress and displacement continuity between this solution and the cohesive zone at $x = l/2$, and uses the resulting conditions to derive an equation for $\delta_c(t)$. The result is:

$$\boxed{\delta_c'(t)+\frac{\delta_c(t)}{\tau}\exp\left(1-\frac{2\delta_c(t)}{\delta^*}\right)=c\,\dot{\varepsilon}_0\,t-2\delta_c^{(1)\prime}\left(t-\frac{2l}{c}\right)-2\delta_c^{(2)\prime}\left(t-\frac{l}{c}\right),\ \text{valid for } 2\frac{l}{c}\le t\le 3\frac{l}{c}} \tag{23a}$$

to be solved with the initial condition:

$$\boxed{\delta_c\left(\frac{2l}{c}\right)=\delta_c^{(2)}\left(\frac{2l}{c}\right)}, \tag{23b}$$

where $\delta_c^{(2)}(t)$ is the solution to (22). Comparing (22) to (23), it is clear by induction what the governing differential equation for $\delta_c(t)$ will be for any later time range.

Interestingly, by comparing (17), (22), (23) and the general form obtained by induction, one observes that a differential delay equation can be derived for $\delta_c(t)$ after any number of reflections in terms of only the $\delta_c(t)$ solution from the regime involving one less reflection. Thus, for the equation giving $\delta_c^{(n+1)}(t)$, the right side of the equation for $\delta_c^{(n)}(t)$, when written by replacing t by $t + l/c$, is employed to eliminate all prior $\delta_c(t)$ terms except those involving $\delta_c^{(n)}(t)$. The result is, valid for $n \ge 1$ reflections [the initial pre-reflection regime is governed by (17)]:

$$\boxed{\begin{aligned}\delta_c^{(n+1)'}(t)+\frac{\delta_c^{(n+1)}(t)}{\tau}\exp\left(1-\frac{2\delta_c^{(n+1)}(t)}{\delta^*}\right)&=\dot{\varepsilon}_0 l-\delta_c^{(n)'}\left(t-\frac{l}{c}\right)\\&+\frac{\delta_c^{(n)}(t-l/c)}{\tau}\exp\left(1-\frac{2\delta_c^{(n)}(t-l/c)}{\delta^*}\right),\qquad n\frac{l}{c}\le t\le(n+1)\frac{l}{c}\end{aligned}} \tag{24a}$$

to be solved with the initial condition:

$$\boxed{\delta_c^{(n+1)}\left(n\frac{l}{c}\right)=\delta_c^{(n)}\left(n\frac{l}{c}\right)}. \tag{24b}$$

3. Model Assuming Initially Unflawed Material

We shall first propose and analyze a model that treats the material as an initially flaw-free homogeneous, isotropic linear elastic solid which develops microscopic flaws (represented by cohesive zones) at the times and locations predicted by a dynamic instability analysis. Our specific goal is to predict the minimum fragment size, and the time of fragmentation initiation (i.e., instability onset), as a function of strain rate and material properties.

As just noted, there are two unknowns to be determined: the time of fragmentation initiation, and the minimum fragment size. We impose two simultaneous conditions to determine these unknowns. First, we hypothesize that fragmentation initiation will occur as soon as it is first possible, and that this is at the time t_{cr} when the stress level in the cohesive zone has just reached the cohesive strength. In terms of the cohesive zone displacement, this requires

$$\boxed{2\delta_c(t_{cr})=\delta^*}. \tag{25}$$

Second, the instability condition determining the minimum possible fragment size, l_{min}, is the requirement that at time t_{cr}, the prospective brittle fragment, which is the elastic segment of Section 2, has just stopped expanding. This requires, applying (11) for $\delta_s(t)$ in terms of $\delta_c(t)$:

$$\boxed{\delta_s'(t_{cr}) = 0 \quad \Rightarrow \quad \delta_c'(t_{cr}) = \dot{\varepsilon}_o \frac{l_{\min}}{2}}. \tag{26}$$

We begin with very high strain rate situations, for which the analysis is simplest, and then show how to generalize the analysis to treat lower strain rates.

3.1 *Formulation for Very High Strain Rates*

The dynamic fragmentation analysis is simplest when t_{cr} is shorter than the time it takes an elastic wave to traverse the length of the minimum elastic segment size, l_{min}/c, so that (17) applies. We refer to this as the very high strain rate regime. In this regime, combining (25) and (26), and employing (17) to express $\delta_c'(t)$, we find the minimum fragment size to be

$$\boxed{l_{\min} = 2c\left(t_{cr} - \frac{1}{\dot{\varepsilon}_o}\frac{\sigma_{\max}}{\hat{E}}\right), \qquad \text{valid for } \; 0 \le t_{cr} \le \frac{l_{\min}}{c}}, \tag{27}$$

where t_{cr} is obtained by solution of (25) [which in turn requires the numerical solution of (17)].

3.2 *A Linearized Analysis of the Very High Strain Rate Regime*

The results (27) with (25), relying as they do on the numerical solution to the nonlinear differential equation (17), are not entirely transparent. Thus, before obtaining solutions to them for a range of strain rates, we shall solve a linearized version of the problem, to obtain a more physical understanding of the results.

To linearize, note that the second term in (17) consists of a linear function multiplied by an exponential. We shall need the solution to this equation until condition (25) is satisfied – i.e., until the peak in Figure 4 is reached. This suggests that a reasonable linearization is to eliminate the exponential term in (17); this corresponds to a cohesive zone stress-displacement relation that is a straight line from the origin through the maximum of the curve illustrated in Figure 4 – i.e., a secant line. The resulting linearized version of (17) is:

$$\delta_c'(t) + \frac{1}{\tau}\delta_c(t) = c\,\dot{\varepsilon}_0\,t, \qquad \text{valid for } \; 0 \le t \le \frac{l}{c}\ . \tag{28}$$

The general solution to (28) is, having applied the initial condition $\delta_c(0) = 0$:

$$\delta_c(t) = c\dot{\varepsilon}_0\tau^2\left(\frac{t}{\tau} + e^{-t/\tau} - 1\right). \tag{29}$$

Application of condition (26) to this gives the following result for minimum fragment size:

$$\boxed{l_{\min} = \frac{\delta^*\hat{E}}{\sigma_{\max}}\left(1 - e^{-t_{cr}/\tau}\right), \qquad \text{valid for } \; 0 \le t_{cr} \le \frac{l_{\min}}{c}.} \tag{30}$$

Application of (25) to (29) results in the following implicit equation for t_{cr}:

$$\boxed{\frac{t_{cr}}{\tau} + e^{-t_{cr}/\tau} - 1 = \frac{1}{\tilde{\dot{\varepsilon}}_0}, \qquad \text{where} \quad \tilde{\dot{\varepsilon}}_0 \equiv \frac{\dot{\varepsilon}_0\tau}{\sigma_{\max}/\hat{E}}.} \tag{31}$$

The result (30) is indeed more transparent than the exact result (21): it shows explicitly that for deformations in the high strain rate regime, the minimum fragment size scales with the material parameter group $\left(\delta^*\hat{E}/\sigma_{\max}\right)$, and that this group provides an upper bound on the minimum fragment size in the high strain rate regime [all within the linearized analysis, of course].

3.3 *Solution to the Nonlinear Problem for Very High Strain Rates*

We now return and derive the results for the full nonlinear problem set up in Section 3.1. We shall first nondimensionalize these equations, so that the solutions can be presented for arbitrary materials. Define the nondimensional quantities:

$$\tilde{\delta}_c\left(\tilde{t}\right) \equiv \frac{\delta_c(t)}{\delta^*/2}, \qquad \tilde{t} \equiv \frac{t}{\tau}, \quad \tilde{l} \equiv \frac{l}{c\tau} \qquad \Rightarrow \qquad \tilde{\delta}_c'\left(\tilde{t}\right) = \frac{\tau\delta_c'(t)}{\delta^*/2}, \tag{32}$$

where a prime denotes differentiation with respect to a function's argument, and the chain rule was used to derive the last of (32). Then, employing τ and $\tilde{\dot{\varepsilon}}_0$ as defined in (18) and (31), equations (17), (25), (27) may be rewritten as, respectively:

Table 1. Nonlinear and linearized solutions for the very high strain rate regime.

	Nonlinear		Linearized	
$\tilde{\dot{\varepsilon}}_o$	$\tilde{l}_{\min}$	$\tilde{t}_{cr}$	$\tilde{l}_{\min}$	$\tilde{t}_{cr}$
0.9120	2.193	2.193	1.717	1.955
1	2.116	2.058	1.683	1.841
2	1.608	1.304	1.397	1.198
3	1.361	1.014	1.222	0.9444
5	1.095	0.7473	1.014	0.7068
10	0.8058	0.5029	0.7664	0.4832
15	0.6702	0.4018	0.6442	0.3888
20	0.5869	0.3435	0.5676	0.3338

$$\tilde{\delta}_c'(\tilde{t}) + \tilde{\delta}_c(\tilde{t}) \exp\left[1 - \tilde{\delta}_c(\tilde{t})\right] = \tilde{\dot{\varepsilon}}_o \, \tilde{t}, \qquad \tilde{\delta}_c(0) = 0, \qquad \text{valid for } \; 0 \le \tilde{t} \le \tilde{l} \tag{33}$$

$$\tilde{\delta}_c(\tilde{t}_{cr}) = 1 \tag{34}$$

$$\tilde{l}_{\min} = 2\left(\tilde{t}_{cr} - \frac{1}{\tilde{\dot{\varepsilon}}_o}\right), \qquad \text{valid for } \; 0 \le \tilde{t}_{cr} \le \tilde{l}_{\min} \; . \tag{35}$$

To solve these, (34) is applied to the numerical solution of (33) to determine $\tilde{t}_{cr}$, which is then employed in (35) to determine $\tilde{l}_{\min}$. The results are presented in Table 1, beginning with the lowest $\tilde{\dot{\varepsilon}}_o$ for which these equations are valid (i.e., delimiting the lower bound of dimensionless strain rate in the high strain rate regime). Dimensioned results for a specific material will be presented later, and these will be compared to the results of other models of dynamic fragmentation.

As a matter of interest, the results of the *linearized* analysis of the previous section can be expressed in terms of the dimensionless quantities defined in (32) as:

$$\tilde{l}_{\min} = 2\left(1 - e^{-\tilde{t}_{cr}}\right), \qquad \text{valid for } \; 0 \le \tilde{t}_{cr} \le \tilde{l}_{\min} \tag{36}$$

$$\tilde{t}_{cr} + e^{-\tilde{t}_{cr}} - 1 = \frac{1}{\tilde{\dot{\varepsilon}}_o}.$$

These linearized results are also shown in Table 1. The linearized results consistently underestimate the full nonlinear solutions, but are reasonably accurate (within ≈ 10%) for $\tilde{\dot{\varepsilon}}_o > 3$.

It is interesting to note that the nonlinear results for the high strain rate regime, summarized in Table 1, are very accurately fit (coefficient of determination $R^2 = 0.99921$) by the equation

$$\boxed{\tilde{l}_{\min} = 2.1395\,\tilde{\dot{\varepsilon}}_o^{-0.4264}} \quad . \tag{37}$$

3.4 *Solution for Lower Strain Rates*

We have just shown that the preceding analysis is valid for normalized strain rates of $\tilde{\dot{\varepsilon}}_o = 0.9120$ and higher. For lower strain rates, this analysis implies that t_{cr} will be longer than it takes for an elastic wave to traverse the length of the minimum elastic segment size, l_{min}/c, so that (17) will not be valid. In order to be able to use the simple model in this lower strain rate regime, we assume that before instability is attained, narrow regions of higher strain rate begin to develop, i.e., flaws begin to form. Although we do not yet know the locations of these nonuniformities or flaws, we treat them as cohesive zones (since in these regions the material is sufficiently strained that its response has become nonlinear); the analysis finally provides their spacing when the dynamic instability criterion is met. Incidentally, this analysis also provides the fragment size for initially flawed material whose flaw spacing coincides with the fragment size. [Later, in Sections 4 and 6, we shall analyze the effects of different initial flaw spacings.] This assumption that flaws begin to form well before fragmentation instability is attained appears to be supported by the micromechanics-based large-scale numerical modeling of Curran and Seaman (1996), which models in detail the evolution of microscopic damage and the development of fragmentation in brittle materials. These authors observe that the evolution of microcrack damage begins very early in the loading process. They also observe that the stress does not reach its peak until much later in the process, when a kind of “avalanche” occurs, which

appears to support our hypothesis that fragmentation instability does not occur until the stress attains its maximum value.

Notice that the differential equation (22a) for $\delta_c(t)$ in the range $l/c \le t \le 2l/c$ [and all ensuing differential equations for $\delta_c(t)$ for longer fragmentation times] depends on the fragment size l, unlike the differential equation (17) for the high-strain-rate regime. In that case, the time at which an instability is first possible was given by (25), which is independent of fragment size; the minimum possible fragment size was then determined from (27) using the critical time calculated from (25). Here, we must solve the two fragmentation initiation conditions (25) and (26) *simultaneously*. Furthermore, now $\delta_c(t)$ in these conditions refers to the solution of (22a), or, more generally, (24a), all of which depend on l.

To solve for the fragment size and time to fragmentation initiation, we first nondimensionalize the equations just mentioned in the same manner employed in Section 3.3. Thus, (25) and (26) become:

$$\tilde{\delta}_c(\tilde{t}_{cr}) = 1, \qquad \tilde{\delta}_c'(\tilde{t}_{cr}) = \tilde{\dot{\varepsilon}}_0 \frac{\tilde{l}_{\min}}{2}, \tag{38a, b}$$

and (17) and (24) become:

$$\tilde{\delta}_c^{(1)'}\left(\tilde{t}\right) + \tilde{\delta}_c^{(1)}(\tilde{t}) \exp\left[1 - \tilde{\delta}_c^{(1)}(\tilde{t})\right] = \tilde{\dot{\varepsilon}}_0 \, \tilde{t}, \qquad \tilde{\delta}_c^{(1)}(0) = 0, \qquad \text{valid for } \; 0 \le \tilde{t} \le \tilde{l} \;, \tag{39}$$

$$\begin{gathered} \tilde{\delta}_c^{(n+1)'}\left(\tilde{t}\right) + \tilde{\delta}_c^{(n+1)}(\tilde{t}) \exp\left(1 - \tilde{\delta}_c^{(n+1)}(\tilde{t})\right) = \tilde{\dot{\varepsilon}}_0 \tilde{l} - \tilde{\delta}_c^{(n)'}\left(\tilde{t} - \tilde{l}\right) + \tilde{\delta}_c^{(n)}(\tilde{t} - \tilde{l}) \exp\left(1 - \tilde{\delta}_c^{(n)}(\tilde{t} - \tilde{l})\right), \\ \tilde{\delta}_c^{(n+1)}\left(n\tilde{l}\right) = \tilde{\delta}_c^{(n)}\left(n\tilde{l}\right), \qquad \text{valid for } \; n\tilde{l} \le \tilde{t} \le (n+1)\tilde{l}, \quad n \ge 1. \end{gathered} \tag{40}$$

The above system is solved for fragment size and time of fragmentation initiation by simultaneous solution of (38), with (39) and the appropriate member(s) of (40), depending on the applied strain rate. The nonlinear differential equations (39) and (40) require very accurate numerical solution in order that correct results be obtained. We employed Mathematica with 24 digits of working precision to obtain satisfactory results. For strain rates lower than $\tilde{\dot{\varepsilon}}_0 = 0.9120$, we have found that $\tilde{t}_{cr}$ next lies in the range $2\tilde{l} < \tilde{t}_{cr} < 3\tilde{l}$. The results for this lower strain rate regime are given in Table 2, where we also indicate the number of wave reflections before

instability is attained. It is interesting to note that the results in Table 2 having two wave reflections before fragmentation onset are very accurately fit (coefficient of determination $R^2 = 0.99995$) by the equation

$$\boxed{\tilde{l}_{\min} = 1.2999\,\tilde{\dot{\varepsilon}}_o^{-0.66671}}\,. \tag{41}$$

Considering the results (37) and (41) together, our model predicts that the minimum fragment size is proportional to strain rate to the –0.4264 power in the very high strain rate regime ($\tilde{\dot{\varepsilon}}_o \geq 0.9120$), which changes to the –0.6667 power for the portion of the lower strain rate regime in which fragmentation onset occurs after two wave reflections. These conclusions are quite similar to those resulting from the micromechanics-based large-scale numerical modeling of Curran and Seaman (1996), who found fragment size to be proportional to strain rate to a power ranging from about –0.3 to –0.6 for the highest strain rates they examined, and to a power closer to –0.75 for lower strain rates.

Table 2. Nonlinear solution for the lower strain rate regime.

$\tilde{\dot{\varepsilon}}_o$	$\tilde{l}_{\min}$	$\tilde{t}_{cr}$	wave reflections before fragmentation onset
0.9120	2.193	2.193	0
0.9	1.398	2.885	2
0.8	1.509	3.105	2
0.7	1.648	3.379	2
0.6	1.824	3.729	2
0.5	2.059	4.203	2
0.4	2.393	4.882	2
0.3	2.908	5.954	2
0.2	2.715	8.977	3
0.1	3.450	15.98	4
0.09	3.806	17.31	4
0.08	3.397	20.14	5
0.07	3.778	22.17	5
0.06	4.131	24.95	6
0.05	4.225	29.81	7
0.04	5.000	35.33	7
0.03	4.888	47.28	9

3.5 *Analysis of the Quasi-Static Strain-Rate Regime*

When the imposed strain rate is sufficiently low, numerous wave reflections occur in an elastic segment prior to fragmentation initiation, meaning that a quasi-static state is approached. For such low strain rates a direct quasi-static analysis of minimum fragment size and time to fragmentation onset becomes possible, as performed here.

Since the inertia term becomes negligible in this case, the conservation of linear momentum (3) reduces to:

$$\frac{\partial \sigma_{xx}}{\partial x} = 0 \quad \Rightarrow \quad \sigma_{xx}(x,t) = h(t), \tag{42}$$

where $h(t)$ is an undetermined function of integration. Using (42) in (4) and integrating with respect to x gives:

$$\hat{E}\frac{\partial u}{\partial x} = h(t) \quad \Rightarrow \quad u(x,t) = \frac{h(t)}{\hat{E}}x, \tag{43}$$

the resulting function of integration having been set to zero since $u(0,t) = 0$.

Stress continuity with the cohesive zone, (13), applied to (43) gives

$$h(t) = F\big(2\delta_c(t)\big). \tag{44}$$

Displacement continuity with the cohesive zone, (11), applied to (43) with (44) results in the following equation for $\delta_c(t)$:

$$\delta_c(t) + \frac{l}{2\hat{E}}F\big(2\delta_c(t)\big) = \dot{\varepsilon}_0\frac{l}{2}t. \tag{45}$$

For the present cohesive zone model (16), this becomes

$$\delta_c(t)\left[1 + \frac{l\sigma_{\max}}{\delta^*\hat{E}}\exp\left(1 - \frac{2\delta_c(t)}{\delta^*}\right)\right] = \dot{\varepsilon}_0\frac{l}{2}t, \tag{46}$$

the time derivative of which gives

$$\delta_c'(t) = \frac{\dot{\varepsilon}_o l/2}{1+\frac{l\sigma_{\max}}{\delta^* \hat{E}}\left(1-\frac{2\delta_c(t)}{\delta^*}\right)\exp\left(1-\frac{2\delta_c(t)}{\delta^*}\right)}. \tag{47}$$

Now we impose the fragmentation initiation conditions (25) and (26). Application of (25) to (46) results in

$$t_{cr} = \frac{1}{\dot{\varepsilon}_o}\left(\frac{\delta^*}{l}+\frac{\sigma_{\max}}{\hat{E}}\right). \tag{48}$$

Use of (25) in (47) at $t = t_{cr}$ shows that (47) satisfies (26) identically. Thus, an additional fragmentation condition is needed to determine the minimum fragment size in the quasi-static regime. Noting that the second term in the denominator of (47) is negative for $t > t_{cr}$, it is clear that for large l values, $\delta_c'(t)$ will become infinite, indicating a fragmentation instability, shortly after $t > t_{cr}$. To determine the minimum l for which $\delta_c'(t)$ will become infinite, one derives that the second term in the denominator of (47), regarded as a function of $\delta_c(t)$, attains a maximum magnitude when $\delta_c(t) = \delta^*$. The minimum l corresponding to a fragmentation instability in the quasi-static regime is thus the one causing the denominator in (47) to vanish when $\delta_c(t) = \delta^*$, namely:

$$\boxed{l_{\min} = \frac{e\delta^* \hat{E}}{\sigma_{\max}}} \quad \Rightarrow \quad \boxed{\tilde{l}_{\min} = 2e}, \tag{49}$$

where e is the natural logarithm base. Substitution of the first of these into (48) gives the time to fragmentation initiation as:

$$\boxed{t_{cr} = \frac{1}{\dot{\varepsilon}_o}\frac{\sigma_{\max}}{\hat{E}}\left(1+e^{-1}\right)} \quad \Rightarrow \quad \boxed{\tilde{t}_{cr} = \frac{1}{\tilde{\dot{\varepsilon}}_o}\left(1+e^{-1}\right)}. \tag{50}$$

These results imply that the minimum fragment size becomes independent of applied strain rate once the quasi-static regime is reached, and that the critical time to fragmentation initiation in this regime is directly proportional to the inverse of the applied strain rate.

3.6 *Alternate Analysis of the Quasi-Static Strain-Rate Regime: Power Balance*

Here we briefly show an alternate analysis of the quasi-static regime that employs a dynamic instability analysis of the governing equations derived via a power balance. We require that the power input to a prospective fragment equal the time rate of change of the kinetic plus potential energy of the fragment:

$$P_{\text{input}} = \frac{\mathrm{d}}{\mathrm{d}t}(T+V). \tag{51}$$

With respect to Figure 2, and writing each term in (51) per unit cross-sectional area of the fragment, we have for the kinetic and potential energies, respectively

$$T = 2\int_0^{l/2} \tfrac{1}{2}\rho \dot{u}^2 \mathrm{d}x = \int_0^{l/2} \rho\left(\frac{x\dot{\delta}_s}{l/2}\right)^2 \mathrm{d}x = \tfrac{1}{6}\rho l \dot{\delta}_s^2, \tag{52}$$

$$V = \frac{1}{2}\hat{E}\left(\frac{\delta_s}{l/2}\right)^2 l + 2\int_0^{\delta_c} F(2\delta_c)\mathrm{d}\delta_c. \tag{53}$$

In deriving (52) and (53), we have assumed that the velocity distribution in the elastic segment is linear with position x; it is this assumption [justified by (43)] that restricts the present analysis to being quasi-static. Writing the total power input per unit cross-sectional area as $2F(2\delta_c)\dot{\delta}$, (51) becomes:

$$2F(2\delta_c)\dot{\delta} = \frac{\rho l}{3}\dot{\delta}_s\ddot{\delta}_s + \frac{4}{l}\hat{E}\delta_s\dot{\delta}_s + 2F(2\delta_c)\dot{\delta}_c, \tag{54}$$

which via $\delta = \delta_s + \delta_c$ simplifies to

$$\frac{\rho l}{6}\ddot{\delta}_s + \frac{2}{l}\hat{E}\delta_s = F(2\delta - 2\delta_s). \tag{55}$$

For a given $\delta(t)$, this equation has a solution for δ_s, say $\hat{\delta}_s$, which satisfies all initial and boundary conditions. Let us perturb this solution with a small perturbation $\xi(t)$ and examine the conditions under which this perturbation can grow. Substitution of $\delta_s = \hat{\delta}_s + \xi(t)$ into (55) gives, neglecting higher-order terms:

$$\frac{\rho l}{6}\ddot{\xi} + \left[\frac{\hat{E}}{l} + F'\left(2\delta - 2\hat{\delta}_s\right)\right]2\xi = 0. \tag{56}$$

The amplitude of ξ will grow rapidly, regardless of its initial size, if its coefficient in (56) is negative; thus, the instability condition for the elastic segment is when this coefficient just vanishes:

$$\frac{\hat{E}}{l} + F'\left(2\delta - 2\hat{\delta}_s\right) = 0. \tag{57}$$

The minimum segment size occurs when F' takes its largest negative value, which for the cohesive zone model (16) is $-\sigma_{\max}/(e\delta^*)$; using this in (57) shows the minimum fragment size to be

$$\boxed{l_{\min} = \frac{e\delta^*\hat{E}}{\sigma_{\max}}}. \tag{58}$$

Observe that this is identical to the size (49) derived by the quasi-static version of the method employed in this paper.

4. Model of Material Containing Pre-Existing Flaws

In this section, we propose a second model of dynamic fragmentation of brittle materials. This model accounts for pre-existing flaws in the material and predicts, on the basis of a dynamic instability analysis, which of these flaws lead to fragmentation (hence the fragment size) and when. At least in this initial analysis, the flaw spacing is assumed to be approximately uniform, so that analytical predictions based on the formulation of Section 2 can be made. In materials for which the initial flaw spacing is not uniform, the present model can be applied to the average initial flaw spacing, and thus can be expected to predict the minimum average fragment size.

Specifically, we again consider a long bar experiencing one-dimensional plane strain dynamic deformation that is a rapid uniform expansion until fragmentation initiates, as described in Section 2. We again focus attention on a prospective brittle fragment. However, in contrast to the model in Section 3, the prospective fragment is now assumed to consist of a number of elastic segments separated by

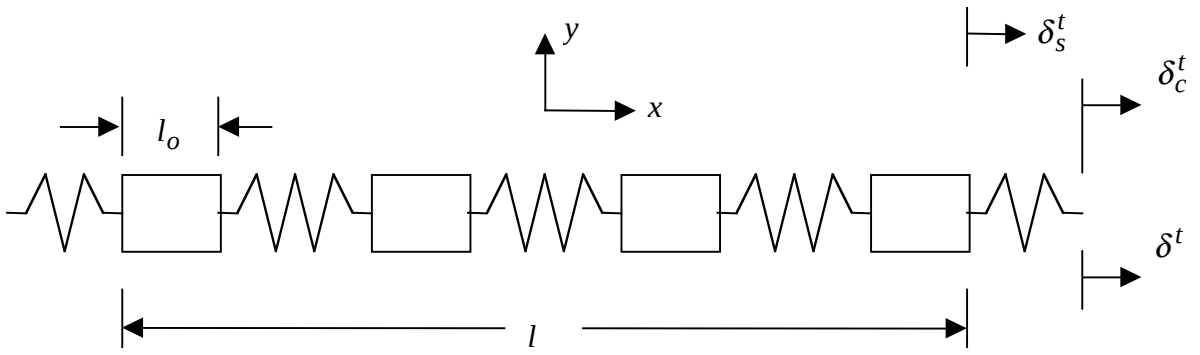

Figure 5. A prospective fragment of length l (to be determined) in material having initial flaw spacing l_o.

cohesive zones (which model the pre-existing flaws), with the size of these segments being the initial flaw spacing in the material. Such a prospective fragment is illustrated in Figure 5. As shown there, l is the length of the prospective brittle fragment and l_o is the length of the elastic subsegments, i.e., the initial flaw spacing. The quantities δ_s^t, δ_c^t and δ^t have the same meanings with respect to the *total* fragment as before, whereas those same quantities without superscript now refer to each subsegment of the total prospective fragment.

Since we are analyzing a prospective fragment under the conditions that the bar is experiencing a uniform rapid expansion until fragmentation initiates, it is clear that the cohesive zone displacements for the subsegments and the prospective fragment are identical until fragmentation initiation:

$$\delta_c^t(t) = \delta_c(t). \tag{59}$$

As in the model of Section 3, we hypothesize that fragmentation cannot initiate until the stress in the cohesive zone reaches the cohesive strength which, via (59), requires in terms of cohesive zone displacement

$$\boxed{\delta_c(t_{cr}) = \delta^*/2}. \tag{60}$$

The instability condition that determines the minimum possible fragment size, l_{min}, is that the fragment has just stopped expanding. Adapting the arguments of Section 3 to the present model, applying (59), we find:

$$\delta_s^t(t) = \dot{\varepsilon}_0 \frac{l}{2} t - \delta_c^t(t) = \dot{\varepsilon}_0 \frac{l}{2} t - \delta_c(t). \tag{61}$$

Thus the instability condition is:

$$\boxed{\delta_s^{t\prime}(t_{cr}) = 0 \quad \Rightarrow \quad \dot{\varepsilon}_0 \frac{l_{\min}}{2} = \delta_c{}'(t_{cr})}. \tag{62}$$

The difference between the present model and that of Section 3 is in how $\delta_c(t)$ must be calculated. For very high strain rates, it may turn out that the minimum fragment size will be the same as the initial flaw spacing. However, in general, one must solve for $\delta_c(t)$ for a span of time involving one or more reflections of elastic waves within the elastic subsegments before fragmentation initiates.

Specifically if, for a very high strain rate, fragmentation initiates at a time $t_{cr} \le l_o / c$, then $\delta_c(t)$ is given by the solution of

$$\delta_c'(t) + \frac{2c\sigma_{\max}}{\delta^* \hat{E}} \delta_c(t) \exp\left[1 - \frac{2}{\delta^*} \delta_c(t)\right] = c\dot{\varepsilon}_0 t, \quad \delta_c(0) = 0, \quad \text{valid for } 0 < t < \frac{l_o}{c}. \tag{63}$$

For strain rates lower than this, we must obtain a solution valid for longer fragmentation initiation times, i.e., for $t_{cr} > l_o / c$. The analysis proceeds in exactly the same manner as that of Section 3.4, except now the elastic segment size is l_o. Nondimensionalizing the instability conditions (60), (62) and the resulting differential equations gives:

$$\tilde{\delta}_c(\tilde{t}_{cr}) = 1, \quad \tilde{\delta}_c'(\tilde{t}_{cr}) = \tilde{\dot{\varepsilon}}_0 \frac{\tilde{l}_{\min}}{2}. \tag{64a, b}$$

$$\tilde{\delta}_c^{(1)\prime}(\tilde{t}) + \tilde{\delta}_c^{(1)}(\tilde{t}) \exp\left[1 - \tilde{\delta}_c^{(1)}(\tilde{t})\right] = \tilde{\dot{\varepsilon}}_0 \tilde{t}, \quad \tilde{\delta}_c^{(1)}(0) = 0, \quad \text{valid for } 0 \le \tilde{t} \le \tilde{l}_o \tag{65}$$

$$\begin{gathered} \tilde{\delta}_c^{(n+1)\prime}(\tilde{t}) + \tilde{\delta}_c^{(n+1)}(\tilde{t}) \exp\left(1 - \tilde{\delta}_c^{(n+1)}(\tilde{t})\right) = \tilde{\dot{\varepsilon}}_0 \tilde{l}_0 - \tilde{\delta}_c^{(n)\prime}(\tilde{t} - \tilde{l}_0) + \tilde{\delta}_c^{(n)}(\tilde{t} - \tilde{l}_0) \exp\left(1 - \tilde{\delta}_c^{(n)}(\tilde{t} - \tilde{l}_0)\right), \\ \tilde{\delta}_c^{(n+1)}(n\tilde{l}_0) = \delta_c^{(n)}(n\tilde{l}_0), \quad \text{valid for } n\tilde{l}_0 \le \tilde{t} \le (n+1)\tilde{l}_0, \quad n \ge 1. \end{gathered} \tag{66}$$

The above system is solved for fragment size and time of fragmentation initiation as follows: for a specified strain rate and initial flaw spacing, $\tilde{\dot{\varepsilon}}_0$ and $\tilde{l}_o$,

one solves (64a) for $\tilde{t}_{cr}$ – this will involve $\tilde{l}_o$, which is known, but not $\tilde{l}_{\min}$. One then uses this in (64b), which gives $\tilde{l}_{\min}$ directly. The minimum fragment size is given by the smallest integer multiple of $\tilde{l}_o$ that is $\geq \tilde{l}_{\min}$. Solutions of this system for a specific material example and specific initial flaw spacings will be provided in Section 6.

5. Review of Two Energy-Balance Models of Dynamic Fragmentation

Perhaps the most widely employed analytical models of dynamic fragmentation in brittle materials are based on rather basic global energy balance arguments. In this section we briefly review the assumptions and analytical predictions of two of the most popular such models.

A pioneering and widely adopted model using energy balance arguments was proposed by Grady (1982). One postulate of this model, which we have adopted here as indicated in Section 2, is that a body is initially in a state of rapid uniform expansion – i.e., the strain rate is constant throughout the body. Grady focused attention on a body portion that would ultimately become a fragment, and decomposed its total kinetic energy into two parts: that of the total mass moving with the center of mass of the body portion, and that associated with relative motion of material particles with respect to the body portion's mass center. He postulated that the latter part of kinetic energy is available to drive fragmentation, and predicted fragment size by equating this energy to that required for the total surface energy to form a new fragment. Miller et al. (1999) have re-derived the Grady model for one-dimensional plane strain deformations of the type considered here. They give the Grady prediction of fragment size as

$$\boxed{l = 24^{\frac{1}{3}}\left(\frac{K_{Ic}}{\rho c \dot{\varepsilon}_0}\right)^{\frac{2}{3}}}, \tag{67}$$

where K_{Ic} is the material's plane strain fracture toughness, ρ is mass density, c is the elastic wave speed (defined earlier for the one-dimensional plane strain deformations treated here) and $\dot{\varepsilon}_0$ is strain rate.

The Grady model was modified by Glenn and Chudnovsky (1986), who argued that both the stored elastic energy of the prospective fragment and its local kinetic energy are available for new fracture surface formation. To apply this energy balance, it is necessary to add the requirement that no fragmentation occurs until the stress attains a critical value, σ_{max}. The resulting prediction for fragment size is

$$\boxed{l = 4\sqrt{\frac{\alpha}{3}}\sinh\left(\frac{\phi}{3}\right)}, \tag{68}$$

where

$$\boxed{\alpha \equiv \frac{3\sigma_{\max}^2}{\hat{E}\rho\dot{\varepsilon}_o^2}, \qquad \beta \equiv \frac{3}{2}\left(\frac{K_{Ic}}{\rho c\dot{\varepsilon}_o}\right)^2, \qquad \phi \equiv \sinh^{-1}\left[\beta(3/\alpha)^{\frac{3}{2}}\right]}. \tag{69}$$

6. Comparison of Present Model Predictions with Previous Models

Let us now compare the predictions of the new analytical mechanics-based models proposed here with the energy-based models just reviewed and also with the numerical finite element simulations of Miller et al. (1999). To facilitate this comparison, and to give a physical feel for the results, we shall analyze a specific material: dense alumina. For this material, Miller et al. (1999) employ the following values for material constants: E = 380 GPa, ρ = 3900 kg/m^3, ν = 0.35, K_{Ic} = 6 MPa$\sqrt{\text{m}}$, σ_{max} = 1 GPa, δ^* = 3.06 × 10^{-8} m. [This δ^* value is computed from $\delta^* = (1-\nu^2)K_{Ic}^2/(eE\sigma_{\max})$, which is derived by applying the J-integral to the cohesive zone model used here, for plane strain linear elastic fracture mechanics.] These result in:

$$c = 12.5\,\text{km/s}, \qquad \hat{E} = 610\,\text{GPa}, \qquad \tau = 7.46\times10^{-10}\,\text{s}. \tag{70}$$

Figure 6 compares the predictions of the Grady (1982) and Glenn and Chudnovsky (1986) models, and the Miller et al. (1999) finite element simulations, with those of the new model assuming initially unflawed material derived in Section 3.

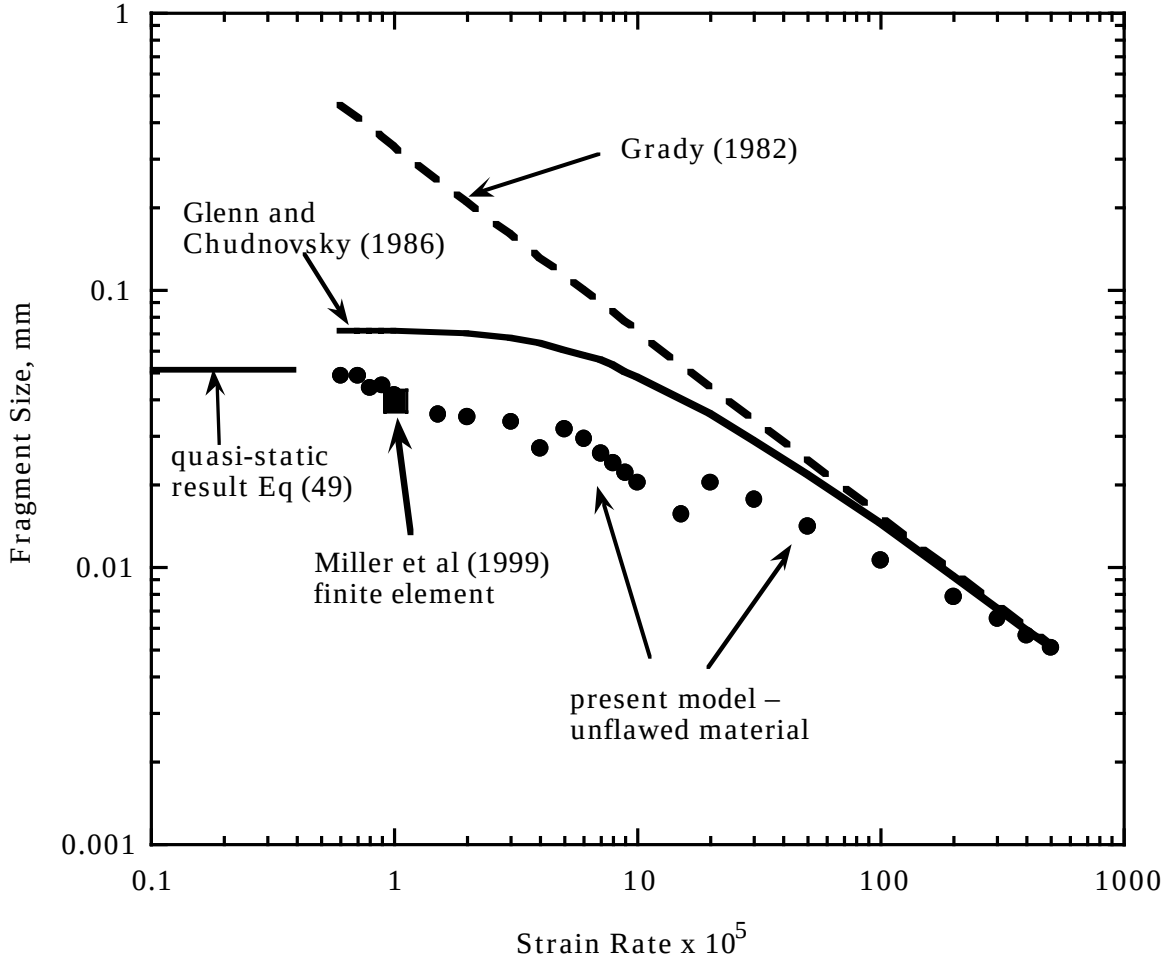

Figure 6. Comparison of several models' predictions of fragment size versus applied strain rate for dense alumina. Results from the model of Section 3 for initially unflawed material are shown as black circles; the closed-form solution of this model in the quasi-static strain rate regime, Eq. (49), is shown as the horizontal line segment indicated.

One very interesting feature of the results shown in Figure 6 is the fact that the predictions of all three models tend to converge at extremely high strain rates. This convergence is a satisfying cross-check on all the models, and it is expected: recall that the energy-balance models of Grady (1982) and Glenn and Chudnovsky (1986) essentially assume that dynamic fragmentation is an instantaneous event, while our new model solves the ongoing dynamic deformation of a brittle material up to the point of fragmentation. By comparing the energy-based model predictions with the new model, one can see clearly over what range of strain rates the assumption that fragmentation is an instantaneous event is a reasonable approximation. The answer is that this is restricted to surprisingly high strain rates.

On the lower end of the range of strain rates presented in Figure 6, notice that the results of the present model are quite close to the numerical finite element result of Miller et al. (1999). As one part of their study on dynamic fragmentation, Miller et al. (1999) performed a numerical finite element simulation of a bar of brittle elastic material that deforms only in the direction of the bar's axis. They also made the Grady (1982) assumption that the bar is in a state of rapid, uniform expansion that remains constant until fragmentation occurs. With reference to Figure 1, Miller et al. (1999) treated a bar of L = 2 mm and h = 0.2 mm, and they applied the boundary and initial conditions described following Figure 1. They modeled the bar as being comprised of linear elastic finite elements that are joined by numerous cohesive zones (either 120 or 480) with the cohesive zone stress-displacement relation of form (16). They performed a dynamic finite element simulation of the bar's behavior, using as a fragmentation criterion that a cohesive zone breaks when its total separation reaches five times the separation at which the cohesive zone stress attains a maximum (see Figure 4), that is, when $2\delta_c = 5\delta^*$. Their result, shown as the black square in Figure 6, is that for 120 cohesive zones in a bar of dense alumina with $\dot{\varepsilon}_0 = 1 \times 10^5$ s^{-1} (having the material constants given in (70) and the paragraph preceding it), which is the sensible one to compare with the present model of initially unflawed material which has a final flaw spacing equal to the fragment size. (This comparison is not exact since final fragments in the Miller et al. (1999) results contain slightly more than one unfractured cohesive zone, on average. We have also analyzed our model of preflawed material for the identical situation treated by Miller et al. (1999); the resulting minimum fragment size is l_{min} = 0.034 mm, just below their *average* fragment size of $\approx$0.040 mm.) Not only is the very good agreement between our results encouraging overall, but note also that Miller et al. (1999) carry out the computation until fragmentation actually occurs, whereas the present model uses the *onset* of dynamic instability to predict fragment size. Thus, this agreement provides another confirmation of the sensibility of our instability criterion.

As noted, the results from the present analysis exhibited in Figure 6 are derived from the model of Section 3, which treats initially unflawed material. Let us now present some sample results from the model of material containing pre-existing

flaws having arbitrary spacing, derived in Section 4. We shall analyze the same dense alumina described at the beginning of this section and explore the effects of several different initial flaw spacings on the predicted fragment size. This is carried out for three strain rates; the results are reported in Table 3. For each strain rate, the first value of the initial flaw size reported in Table 3 is the minimum fragment size predicted by our model of Section 3 for initially unflawed material. Thus, the prediction is that for initial flaw spacings larger than this value, the fragment size will be the same as the smallest initial flaw spacing. Table 3 shows the results for predicted fragment sizes for several values of initial flaw spacings that are smaller than the minimum unflawed material fragment size, and also the number of elastic wave reflections that occurred within each elastic segment between the initial flaws before fragmentation onset was attained. The model prediction of the actual fragment size is the integer multiple of the initial fragment size that is $\geq$ to the predicted l_{min}. For example, when $\dot{\varepsilon}_o = 1 \times 10^6$/s, Table 3 shows that for l_o = .0154 mm, the fragment size will equal this initial flaw spacing, since this is the first integer multiple of initial flaw spacing that is just larger than the predicted l_{min} = .0140 mm. However, for the same strain rate, Table 3 shows that for each of the smaller initial flaw spacings listed, the predicted fragment size is *twice* the initial flaw spacing. That is, the model predicts that not every flaw produces a fracture surface in the actual fragmentation process. We anticipate that if even smaller initial flaw spacings were analyzed, the predicted fragment size would contain even more initial flaws. Both of these conclusions are in accord with the behavior observed in the numerical finite element simulations of Miller et al. (1999).

Table 3. Predicted fragment sizes for initially flawed material (dense alumina) having flaw spacing l_o for three applied strain rates. The actual fragment size prediction is the integer multiple of l_o that is just $\geq l_{min}$.

$\dot{\varepsilon}_o = 5 \times 10^6$/s		
l_o, mm	l_{min}, mm	wave reflections before fragmentation onset
.0142	.0142	0
.0071	.00792	2
.00473	.00648	4
.00355	.00299	7
.00284	.00314	10

$\dot{\varepsilon}_o = 1 \times 10^6$/s		
l_o, mm	l_{min}, mm	wave reflections before fragmentation onset
.0205	.0205	2
.0154	.0140	2
.01025	.0125	5
.00683	.00890	11

$\dot{\varepsilon}_o = 5 \times 10^5$/s		
l_o, mm	l_{min}, mm	wave reflections before fragmentation onset
.0318	.0318	2
.02385	.0194	3
.0159	.0182	5
.0106	.0138	10

7. Strain-Rate Profiles in a Prospective Fragment During Pre-Fragmentation Dynamic Deformation

The method of analysis described in the foregoing, in which we solve explicitly for the time-varying dynamic deformation in a prospective fragment until fragmentation initiates, can be employed to determine the strain rate pointwise in the prospective fragment. Here we show how this is done, and we compute strain rate profiles in a prospective fragment at several times during the deformation prior to fragmentation initiation. This enables an enhanced understanding of the deformation history of a fragment.

The key to the analysis is Figure 3. One first determines the displacement field in each of the labeled regions of that figure; the strain rate field is then determined by calculating the mixed partial derivative of displacement with respect to position and time. We will illustrate the procedure for a few regions in Figure 3, and then simply provide the results for the remaining regions.

Beginning with Region A of Figure 3, we showed that the displacement field everywhere in this region is given by (8); from this, the strain and strain rate fields are calculated by taking partial derivatives with respect to location and then time, respectively. The strain rate in Region A is thus:

$$\dot{\varepsilon}(x,t) = \frac{\partial^2 u(x,t)}{\partial x \partial t} = \dot{\varepsilon}_o . \tag{71}$$

Next, for Region B of Figure 3, we determined that the displacement field is of the form (9), and we showed later that the function $G(\xi)$ appearing in (9) is given by (19). Combining these results gives the displacement field in Region B, and from it we calculate the strain rate field in Region B:

$$u(x,t) = \frac{\dot{\varepsilon}_o}{4c}\left[(x+ct)^2 - (x-ct)^2\right] - \delta_c^{(1)}\left(\frac{1}{c}\left(x+ct-\frac{l}{2}\right)\right) \tag{72a}$$

$$\dot{\varepsilon}(x,t) = \dot{\varepsilon}_o - \frac{1}{c}\delta_c^{(1)''}\left(\frac{1}{c}\left(x+ct-\frac{l}{2}\right)\right). \tag{72b}$$

To calculate the displacement field in Region C of Figure 3, we recall that the general solution form is (6); observe then that in Region C this solution will be the sum of the ($x + ct$) portion of the solution from Region B and the ($x - ct$) portion of the solution from Region B′. The Region B displacement field solution is given by (72a), while an analysis similar to the one leading to that result (or, more simply, application of antisymmetry), shows that the Region B′ displacement field is

$$u(x,t) = \frac{\dot{\varepsilon}_o}{4c}\left[(x+ct)^2 - (x-ct)^2\right] + \delta_c^{(1)}\left(\frac{1}{c}\left(-x+ct-\frac{l}{2}\right)\right). \tag{73}$$

Thus, the procedure just described leads to the following displacement field, and from this the strain rate field, for Region C:

$$u(x,t) = \frac{\dot{\varepsilon}_o}{4c}\left[(x+ct)^2 - (x-ct)^2\right] - \delta_c^{(1)}\left(\frac{1}{c}\left(x+ct-\frac{l}{2}\right)\right) + \delta_c^{(1)}\left(\frac{1}{c}\left(-x+ct-\frac{l}{2}\right)\right) \tag{74a}$$

$$\dot{\varepsilon}(x,t) = \dot{\varepsilon}_o - \frac{1}{c}\delta_c^{(1)\prime\prime}\left(\frac{1}{c}\left(x+ct-\frac{l}{2}\right)\right) - \frac{1}{c}\delta_c^{(1)\prime\prime}\left(\frac{1}{c}\left(-x+ct-\frac{l}{2}\right)\right). \tag{74b}$$

Observe that all of the above solutions involve $\delta_c^{(1)}$, the solution to (17), which is valid for $0 \le t \le l/c$. The procedure for determining the fields in the remaining regions of Figure 3 is the same as that just described, except that one needs to be cognizant of which δ_c solutions are involved. For example, let us consider the solution in Region D. We showed that this has the form (20); the function $H(\xi)$ appearing there can be solved for from (21a), which shows that it will involve both $\delta_c^{(1)}$ and $\delta_c^{(2)}$. Thus, the results for Region D are:

$$\begin{aligned} u(x,t) = \frac{\dot{\varepsilon}_o}{4c}\left[(x+ct)^2 - (x-ct)^2\right] &- \delta_c^{(1)}\left(\frac{1}{c}\left(x+ct-\frac{l}{2}\right)\right) + \delta_c^{(1)}\left(\frac{1}{c}\left(-x+ct-\frac{3l}{2}\right)\right) \\ &+ \delta_c^{(2)}\left(\frac{1}{c}\left(-x+ct-\frac{l}{2}\right)\right) \end{aligned} \tag{75a}$$

$$\dot{\varepsilon}(x,t) = \dot{\varepsilon}_o - \frac{1}{c}\left[\delta_c^{(1)\prime\prime}\left(\frac{1}{c}\left(x+ct-\frac{l}{2}\right)\right) + \delta_c^{(1)\prime\prime}\left(\frac{1}{c}\left(-x+ct-\frac{3l}{2}\right)\right) + \delta_c^{(2)\prime\prime}\left(\frac{1}{c}\left(-x+ct-\frac{l}{2}\right)\right)\right]. \tag{75b}$$

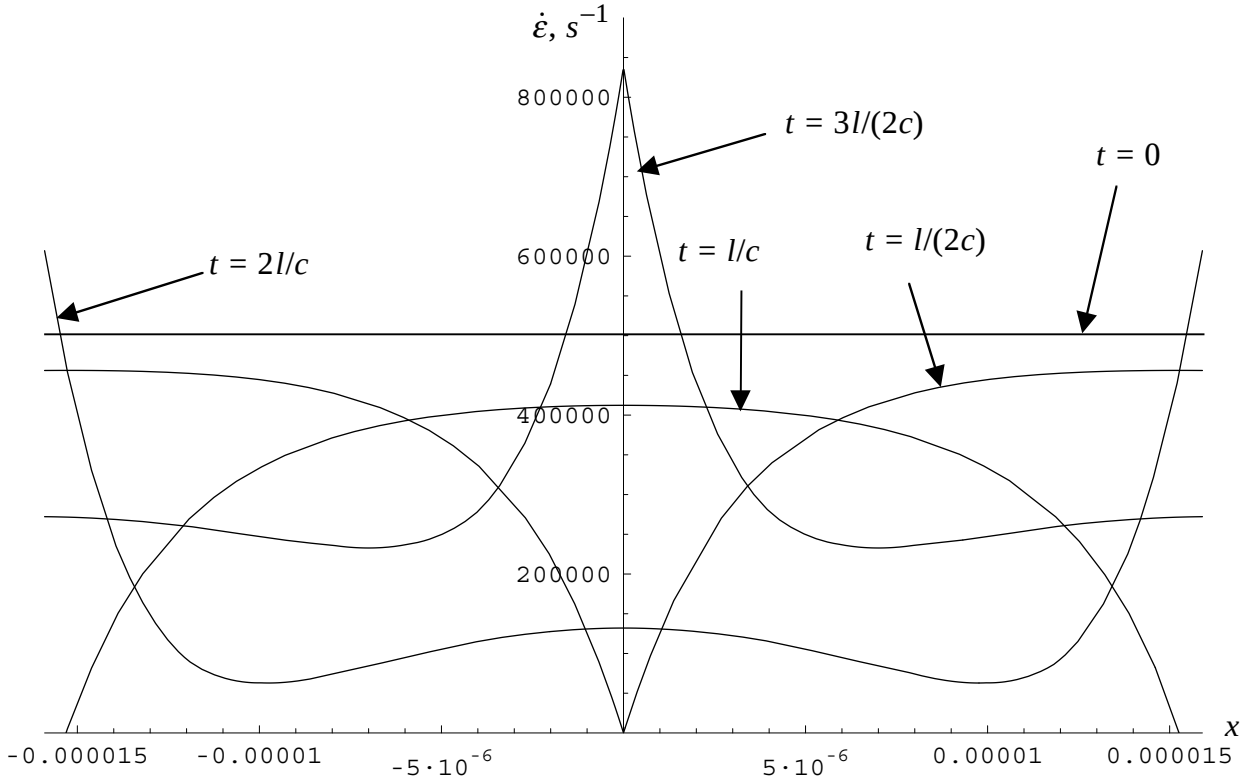

Figure 7. The strain-rate distribution in the elastic segment of a critical-size prospective fragment at five discrete times prior to predicted fragmentation initiation: t = {0, $l/2c$, l/c, 3l/2c, 2l/c}, for an alumina bar experiencing a strain rate of 5×10^5 s^{-1}.

The strain rate field in Region D′ is identical to (75b) if (–x) is replaced with x. The strain rate solutions for the remaining regions shown in Figure 3 are obtained using reasoning like that just outlined; we thus omit them for space reasons.

To get a feeling for what is actually happening within a prospective fragment during the pre-fragmentation initiation period, we plot in Figure 7 the strain rate distribution within the elastic segment of a critical-size prospective fragment for a specific case: an alumina bar deforming at a strain rate of 5×10^5 s^{-1}. This figure shows the strain rate distribution at five times prior to fragmentation initiation; observe that the strain rate is positive everywhere in the elastic segment, and that its distribution is clearly not uniform. In Figure 8 we show the strain rate distribution for the same fragment at two time steps after fragmentation initiation is predicted by our model to have occurred. Observe here that the strain rate is *negative* everywhere within the fragment.

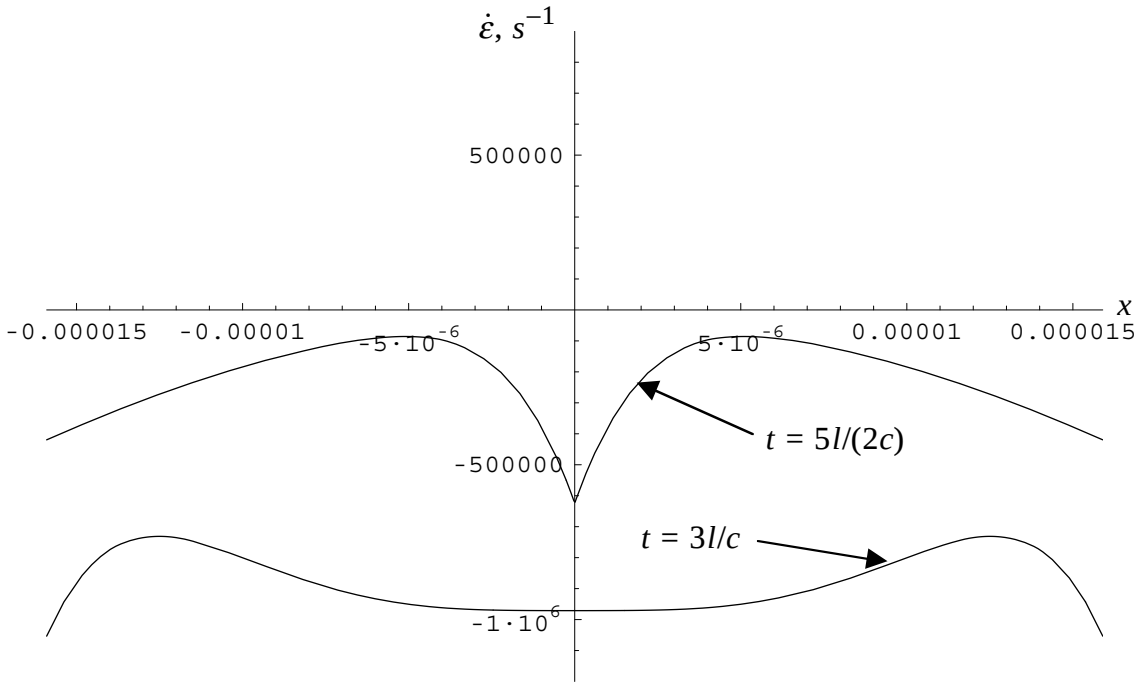

Figure 8. The strain-rate distribution in the elastic segment of a critical-size prospective fragment at two discrete times after predicted fragmentation initiation: t = {5*l*/2*c*, 3*l*/*c*}, for an alumina bar experiencing a strain rate of 5 x 10^5 s^{-1}.

One interesting conclusion to be drawn from the strain rate profiles displayed in Figure 7 is that a simplified model, in which one assumed that the fragment's strain rate was uniform or nearly so from deformation initiation until fragmentation onset, would be seriously in error: the exact results for the strain rate distribution show that it is far from uniform throughout this time span. Figure 8 confirms the sensibility of our criterion that fragmentation initiates when the elastic segment just stops expanding: it shows that the elastic segment indeed continues to contract, and with an increasing rate, as time progresses beyond the predicted fragmentation initiation time.

8. Generalization of Models to Three-Dimensional Deformations

For simplicity of presentation, the modeling described thus far has pertained to one-dimensional dynamic deformations of a bar. Here we show that this modeling, and indeed the specific quantitative results, apply directly to three-dimensional dynamic deformations of a brittle solid when the Grady assumption is invoked.

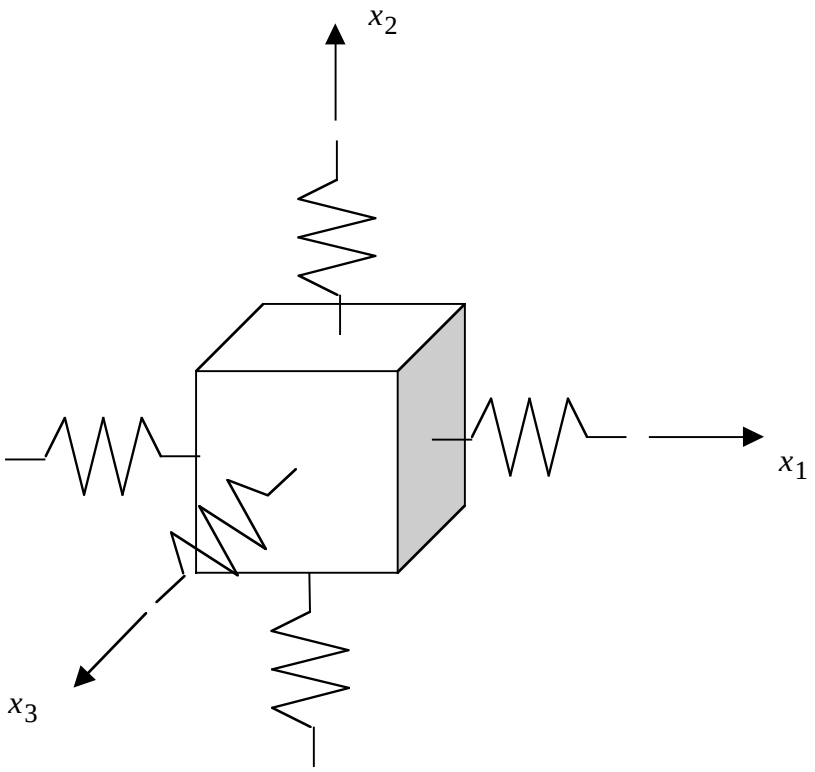

Figure 9. Cubic prospective fragment with cohesive zones.

Recall that the Grady (1982) assumption is that a body is in a state of rapid uniform expansion until fragmentation initiates, so that the strain rate is constant throughout the body. In the one-dimensional deformations considered thus far, this corresponded to the one nonzero component of strain rate being constant throughout the bar [and we solved the dynamic deformation problem to determine how this overall constant strain rate was apportioned between the cohesive zones and the elastic segment of a prospective fragment].

The three-dimensional version of the Grady assumption is that there is a uniform volumetric strain rate, so that, in terms of any Cartesian coordinate system, the shear strain rates are all zero and the normal strain rates are nonzero and equal. The way to generalize our previous analysis to this three-dimensional case is to consider prospective fragments to be cubes that are connected to one another by cohesive zones of the same type considered earlier, as illustrated in Figure 9. Since all normal strain rates are equal, the deformation in each of the three cube directions will be the same, so it is sufficient to analyze one direction.

Using the fact that $\varepsilon_{11} = \varepsilon_{22} = \varepsilon_{33}$, the normal stress–normal strain relation parallel to any cube axis has the form, from (1)

$$\sigma_{11} = \frac{E}{1+\nu}\left[\varepsilon_{11} + \frac{\nu}{1-2\nu}(3\varepsilon_{11})\right] = \frac{E(1-\nu)}{(1+\nu)(1-2\nu)}\varepsilon_{11} \equiv \hat{E}\varepsilon_{11}. \tag{76}$$

Notice that the effective tensile modulus $\hat{E}$ appearing in (76) is identical to that determined in (2) in our previous one-dimensional analysis. Thus, the present 3-D problem is identical in each direction to the 1-D problems already solved, so that the answers already obtained for the 1-D fragment size apply directly to the size of cubic fragments in a three-dimensional uniform volumetric strain rate situation.

9. Discussion

The models introduced in this paper appear to be generalizable to treat dynamic fragmentation in a variety of additional situations and material types beyond those analyzed here. First, these models could be adapted to study fragmentation under different boundary and initial conditions. In the present study, we adopted the Grady (1982) assumption of a body experiencing a uniform, constant strain rate until fragmentation initiates, both to permit direct comparisons of our results with those of previous models, and also because this appears to be the simplest reasonable assumption. However, one can envision other practically important situations that may not be well-modeled by the Grady assumption, such as any which involve highly nonuniform rapid deposition of energy into a body. The present models appear adaptable to the analysis of such situations by imposing different boundary and initial conditions. Second, the present models appear generalizable to fragmentation of other than brittle materials: one could still formulate a wave propagation problem (linear or nonlinear, depending on the material's dynamic response) in a prospective fragment, and join its solution to appropriate cohesive zone behavior as done here. For example, for materials in which the fragmentation event does not simply involve brittle cleavage of atomic

planes, a cohesive model of the actual dynamic interface separation behavior of the material under consideration would be employed.

A possible limitation of the models introduced here is that, since they predict fragment size by analyzing the dynamic instability that causes fragmentation *initiation*, the reversibility or irreversibility of cohesive zone response does not enter the analysis. [The numerical finite element simulations of Miller et al. (1999) assume reversible cohesive zone response until fracture occurs.] The importance of this is an interesting question for future work; one suspects that it may have greater importance in cases of highly nonuniform initial strain rate than in the uniform strain rate case analyzed here.

Acknowledgements

This research was supported by Contract BB-3609 with Sandia National Laboratories, with additional funding by the Lawrence Livermore National Laboratory under contract No. W-7405-ENG-48 with the DOE. Helpful discussions with Professor L. B. Freund of Brown University are gratefully acknowledged, especially his suggestion of the power balance analysis of Section 3.6.

References

Camancho, G. T. and Ortiz, M., 1996. Computational modeling of impact damage in brittle materials. International Journal of Solids and Structures 33, 2899-2938.

Curran, D. R. and Seaman, L., 1996. Simplified models of fracture and fragmentation. In: Davison, L., Grady, D. E., Shahinpoor, M. (Eds.), High-Pressure Shock Compression of Solids II – Dynamic Fracture and Fragmentation. Springer-Verlag, pp. 340-365.

Espinosa, H. D., Zavattieri, P. D. and Dwivedi, S. K., 1998. A finite deformation continuum/discrete model for the description of fragmentation and damage in brittle materials. Journal of the Mechanics and Physics of Solids 46, 1909-1942.

Glenn, L. A. and Chudnovsky, A., 1986. Strain-energy effects on dynamic fragmentation. Journal of Applied Physics 59, 1379-1380.

Grady, D. E., 1982. Local inertial effects in dynamic fragmentation. Journal of Applied Physics 53, 322-325.

Miller, O., Freund, L. B. and Needleman, A., 1999. Modeling and simulation of dynamic fragmentation in brittle materials. International Journal of Fracture 96, 101-125.

Rose, J. H., Ferrante, J. and Smith, J. R., 1981. Universal binding energy curves for metals and bimetallic interfaces. Physical Review Letters 47, 675-678.

Rose, J. H., Smith, J. R. and Ferrante, J., 1983. Universal features of bonding in metals. Physical Review B 28, 1835-1845.